In situ observation of liquid metal dealloying and etching of porous FeCr by X-ray tomography and X-ray diffraction

Morgane Mokhtari, Christophe Le Bourlot, Jérome Adrien, Anne Bonnin, Wolfgang Ludwig, Pierre-Antoine Geslin, Takeshi Wada, Jannick Duchet-Rumeau, Hidemi Kato, Eric Maire

In situ observation of liquid metal dealloying and etching of porous FeCr by X-ray tomography and X-ray diffraction

Morgane Mokhtari[a,b,c,d], Christophe Le Bourlot[a], Jérome Adrien[a], Anne Bonnin[e], Wolfgang Ludwig[a,f],Pierre-Antoine Geslin[a,b], Takeshi Wada[b], Jannick Duchet-Rumeau[c], Hidemi Kato[b], Eric Maire[a]

[a] MATEIS Laboratory, Lyon University, Villeurbanne 69100, France
[b] Institute for Materials Research, Tohoku University, Sendai 980-8577, Japan
[c] IMP Laboratory, Lyon University, Villeurbanne 69100, France
[d]Avignon Université, INRAE, UMR EMMAH, F-84000, Avignon, France
[e] Swiss Light Source, Paul Scherrer Institute, Villigen, Switzerland
[f] European Synchrotron Radiation Facility, Grenoble, France

Abstract
A liquid metal dealloying mechanism is investigated *in situ* using X-ray tomography and X-ray diffraction. While immersing a FeCrNi precursor alloy in a molten Mg bath, a selective dissolution of Ni atoms into the Mg bath occurs leading to FeCr atom rearrangement. At room temperature, after cooling down, a bicontinuous structure of FeCr and a solid solution of Ni in Mg is obtained. A final etching step is used to remove the Mg solid-state solution phase and form microporous FeCr. 3D dealloying and etching kinetics can be measured using X-ray tomography reconstruction. The evolution of relative strain is analyzed from X-ray diffraction patterns. The different behavior observed during dealloying and etching, depending on the precursor composition is discussed.

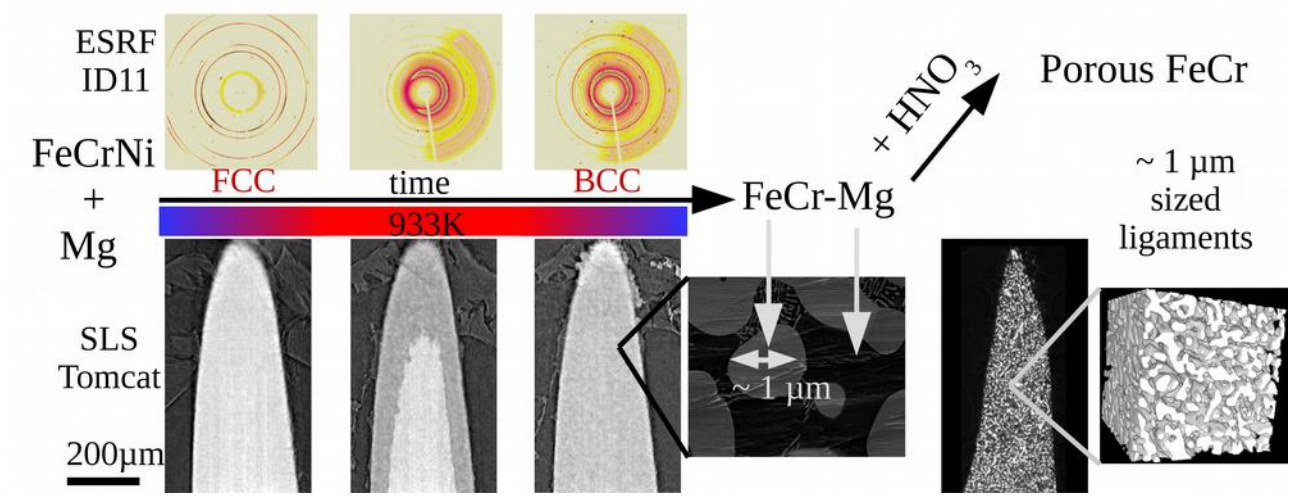

Keywords
dealloying, porous material, Ni alloy, Fe alloy, in *situ* , X-ray tomography, X-ray diffraction

1. Introduction

In the last decades, the attraction of nanoporous metals due to their excellent functional properties have risen [1-4]. Because of their availability, cost and abundance, porous structures of common metals such a-Ti-based, Fe-based...) alloys are highly desired for various applications including energy-harvesting devices [5]. A well-known technique to prepare nanoporous metal is dealloying in an aqueous solution. An attempt was made to dealloy an Fe-Mn precursor in an aqueous solution but the resulting nanoporous Fe was partially oxidized [6]. Because less noble metals are unstable in water, dealloying in an aqueous solution remains challenging. To overcome this limitation, aqueous dealloying was generalized to all liquids and one method based on liquid metalwas developed in [7].

Dealloying with the metallic melt or also called liquid metal dealloying, is a selective dissolution phenomenon from a solid precursor alloy into a metallic melt. Suppose that the precursor is composed of at least two components, one or more being soluble and the others insoluble in the metallic melt. When the solid precursor alloys is immersed in the metallic melt, only atoms of the soluble components dissolve into the melt and the atoms of the insoluble components remain at the melt/precursor interface and spontaneously organize at nanoscale level. After cooling down to room temperature, a bicontinous structure composed by insoluble components and solidified metallic melt (including soluble components) phases is obtained. One phase (in our case the solidified metallic melt) can be removed by selective chemical etching to obtain the final nanoporous material. This technique enables the preparation of nanoporous structures with less noble elements such as pure Ti, Fe, Cr, Nb, Ta, Mg [7-11], alloys (TiCrZr, TiHf, TiZr, TiNb, NiCr, FeCr, stainless steels) [8, 12-18] and non-metals (Si, C) [19,20].
The mechanical properties of these porous materials are controlled by their microstructure (solid phase fraction, ligament size, anisotropy etc.) and are also influenced by the formation of defects appearing during the process. A good understanding of the whole dealloying process is therefore needed to control the final properties of these materials.

Dealloying by free corrosion in an aqueous solution has already been studied by various methods such as *in situ* electrochemical noise or Raman spectroscopy, for example [4, 21-23]. It was even 3D imaged *in situ* to study the evolution of the dealloying front and coarsening and the effect of different parameters on the dealloying process such as precursor composition or acid concentration [24-26]. The fundamentals of dealloying were studied by *in situ* X-ray diffraction of the initial dealloying step of a Cu_3Au precursor [27-30]. Dealloying was followed by *in situ* X-ray diffraction during the whole dealloying process and some residual stresses were measured [31-33]. Contrary to dealloying by free corrosion which occurs at room temperature, the liquid metal dealloying process occurs at high temperature (more than 923K), making the *in situ* observation of the process more difficult, explaining why LMD has not yet been followed *in situ.*

On the other hand, the LMD process has already been studied either by simulation [34] or by post-mortem 2D/3D observations. Moreover, the evolution of a liquid metal dealloying front with dealloying parameters was already studied in 2D, with postmortem SEM observations for different materials Ti, Nb, Ta [10, 35-36], Regarding porous FeCr formation, the evolution of the dealloying front was investigated in 2D in the case of solid metal dealloying [37]. Concerning the etching step, the ligaments and pore size were already 3D imaged before and after the etching step [16,38].

FeCrNi precursors with the same composition as the one used in this analysis have already been studied: after dealloying from a FeCrNi precursor in an Mg melt, the structure was 3D imaged by X-ray tomography [39, 40]. A bicontinous structure in the bulk was obtained when the amount of Ni included is between 30 and 70 at% [39, 40]. However in [40], the process was not monitored experimentally *in situ*.

In materials science, the word microstructure is usually used to describe grain size and crystallographic phases etc. In the case of architectured materials, the word microstructure can also be used to describe the macroscopic arrangement (density, pore size, ligament size etc.). Our material architecture will be referred to as the morphology, and the grain and crystallographic microstrucure will be known as the microstructure.
The morphology was shown to be mainly determined by the dealloying parameters (liquid bath temperature and immersion time). For example, ligament size was independent on the precursor amount of Ni [40]. However, the grain microstructure was totally different depending on the initial Ni amount inside the precursor: a low Ni amount led to the formation of a few large grains while a large amount of Ni induced numerous very small grains [40]. Therefore, to better understand the different phase transformations occurring during liquid metal dealloying, it is very important to follow the process with an *in situ* method.

In this paper we are combining various *in situ* X-ray experimental methods to get a better understanding of the liquid metal dealloying phenomenon. Since measurements of the dealloying process require both high spatial resolution and fast acquisition, the reported experiments are performed at large scale synchrotron facilities. Both steps of the dealloying process are on the one hand, directly imaged by *in situ* X-ray tomography, and on the other, followed by *in situ* X-ray diffraction. The combination of the two different techniques gives a direct insight into not only the evolution of the microstructure and the morphology, but also the strain field evolution. The *in situ* nature of the experiments allows us to monitor the samples though the entire process and prevents any possible ambiguity that could arise from an *ex situ* study.

2. Materials and methods

2.1 Precursors samples preparation

To select suitable precursor alloy composition and metallic melt, mixing enthalpy values are checked. As described in detail in [7], a negative mixing enthalpy corresponds to soluble components and a positive one to insoluble ones.

In this study, we select a FeCrNi precursor alloy; Ni dissolves in liquid Mg while both Fe and Cr are non-dissolvable into Mg. $(FeCr)_{30}Ni_{70}$ and $(FeCr)_{70}Ni_{30}$ ingots are prepared using arc melting as previously described in [8, 40]. Both precursors exhibit a face-centered cubic (FCC) crystal structure with no allotropic transformation bellow 900°C [41-43]. In contrast, the $Fe_{80}Cr_{20}$ targeted composition has a body-centered cubic (BCC) lattice at high temperature; the cooling rate used in the experiment prevents any evolution at low temperature, especially the formation of the gamma-phase [44]. The Mg melting temperature is 923 K and the Ni solubility in Mg liquid is at least 18%. The Ni is quasi non-soluble in solid Mg, therefore, if the Ni density is too high, an eutectic Mg/Mg_2Ni is formed during solidification (visible in Fig. 1(c) in Okulov et al. [45]); both phases have a hexagonal crystalline structure (respectively $P6_3/mmc$ and $P6_222$ for Mg and Mg_2Ni) [46-48].
To reproduce the lab experiment and have an *in situ* observation of the very same laboratory process, we decided to prepare the precursor with the same experimental procedure as used in previous studies [8, 30, 39, 45] which does not include annealing prior to dealloying.
The precursor ingots are cold-rolled with a large reduction factor to obtain a thin plate of material. This plate is cut into slices and polished until a 300 µm precursor tip shape is obtained. The electron backscattered diffraction map of this precursor displays a large amount of stored energy within the microstructure and shows almost no trace of the initial as-cast millimetric microstructure, presented in [40]. This same study also showed that the microstructure after dealloying, with and without a thermal treatment prior to dealloying, are similar.
To ensure the presence of precursor samples on the center of the set-up, precursor tips are fixed with high temperature resistance glue on top of steel sticks, drilled with a 1 mm diameter hole in their center. We observed that Mg clearly reacts locally with the glass tube but we carefully checked that

enough liquid Mg remained in contact with the precursor sample to avoid any influence of the parasitic glass/Mg reaction on the dealloying process. The *in situ* dealloying experiments require a dedicated reactor to handle the liquid magnesium at more than 923 K and a 360° field of view for tomography. It is achieved by encapsulating the precursor and Mg flakes under vacuum in a 2 mm internal diameter quartz tube. An illustration of the set-up is presented on Appendix 1.

2.2 Dealloyed sample preparation

For the *in situ* chemical etching part, the same precursor samples are cut from the cold-rolled plate with a precision micro-cutting machine into rectangular sheets of 20x10x1 mm^3 and dealloyed at a temperature of 1093 K for 1 hr in a Mg melt bath. The EBSD maps in [40] illustrate the characteristic microstructure of a dealloyed sample: a bicontinuous foam with ligament size of around 5 µm. In this case, the average FeCr grain size is around 30µm, which implies that each ligament is a single grain.

The obtained FeCr-Mg composites are cut into a 0.5-1mm x 1cm rectangular rod and then polished into a tip shape. This FeCr-Mg composite sample is introduced in a 5 mm internal diameter polymer capillary with low concentrated nitric acid (4% volume concentration). The dissolution of the solid-state solution of Mg is followed *in situ* by tomography and X-ray diffraction. Porous samples elaborated from $(FeCr)_{30}Ni_{70}$ and $(FeCr)_{70}Ni_{30}$ precursors will be referred to as 30%FeCr and 70%FeCr, respectively.

2.3 X-ray tomography acquisitions

The dealloying and the etching steps are both followed *in situ* by X-ray phase contrast tomography at Tomcat beamline (SLS, PSI, Switzerland), with an energy of 25 keV on a range of 0-180° rotation with an exposure time of 90 ms, and continuous acquisition of 45 s (dealloying 501 projections) and 135 s (etching 1501 projections) respectively. The full volumes are reconstructed from a phase contrast imaging with an isotropic voxel size of 0.32 µm in lateral dimension in an 8 bit floating point using a single distance phase retrieval algorithm [49] and the GridRec reconstruction algorithm [50-52], and are analyzed with Fiji free software [53] using 3D analysis. For calculating dealloying kinetics and ligament/pore size, we use the Fiji “local thickness” function which enables us to precisely measure the thickness of a phase in a 3D image [61]. The average thickness corresponds to the top of the thickness value distribution peak in the image.

For the dealloying part, to ensure a homogeneous specimen temperature, transparent black X-ray painting was applied on the outside of the tubes. A laser heater [54] provided on the Tomcat beamline was used at a power intensity of 16A to heat the sample prior to dealloying. A rough calibration showed that this intensity was just enough to reach a temperature higher than the Mg melting point. Laser heating often results in localized heating but in our case, it was impossible to experimentally control this homogeneity. Note however that our specimen is rather small and that the two lasers used for heating purposes were focused at its tip. As the dealloying process occurs rapidly, there is a risk that Mg flake melting. This was not, however, observed in our experiments and dealloying occurred in a reproducible manner.

2.4 X-ray diffraction acquisitions

The dealloying and the etching steps are both followed *in situ* by transmission X-ray diffraction on the ID11 beamline (ESRF, France) on a 100 µs side window taken at the center of the sample on the top of the tip, with an energy of 35.1 keV, and a ± 1° wobbling movement during acquisitions. The acquisition process comprises 200 ms long exposures followed by 1 s and 10 s breaks for the dealloying and etching steps, respectively (etching kinetics are much slower than those of dealloying). Calibration is carried out using CeO_2 powder. X-ray diffraction ring data is extracted with the caking method in the PyFai software suite [55, 56]. Lattice parameters are extracted using the statistical momentum method, based on the approach exhibited by Groma [57]. An induction heater is used to heat the sample during the dealloying experiment and is stopped to perform the

cooling step. A rough temperature calibration is performed with a thermocouple in contact with a precursor sample inside a quartz crucible (without vacuum encapsulation and Mg). The cooling rate is very difficult to measure precisely but can be estimated at about 17K/s.

2.5 Scanning electron microscopy - electron backscatter diffraction (SEM-EBSD)

$(FeCr)_{30}Ni_{70}$ and $(FeCr)_{70}Ni_{30}$ precursor sheets (cf. Section 2.1) are dealloyed for 3 min at 933 K to obtain partial dealloying and for us to be able to directly observe the dealloyed grain formation. The SEM-EBSD acquisitions are performed on a JEOL 7100F (JEOL, Japan) and are analyzed with Orientation Imaging Microscopy (OIM) analysis software on crossection polished with *Ar* ion beam polisher (EM-3500 Hitachi, Japan).

2.6 Simulation

To better understand the dealloying kinetics observed experimentally, we adapt a simple diffusion model based on [10, 34] to the geometry of the needle-shape samples used in *in situ* experiments. Therefore, the progression of the dealloying front in time, can be modeled cylindrically. Following our previous study [10,34], we consider the sharp-interface problem given by the Fick equation in the dealloyed region (we assume zero diffusion in the precursor) and the Stefan condition giving the velocity of the precursor interface.

$$\frac{\partial c(r,t)}{\partial t} = D\nabla^2 c(r,t), \forall r \in [R(t), R_\infty]$$

$$\frac{dR}{dt} = \frac{D}{c_0 - c_{intf}} \left(\frac{\partial c}{\partial r}\right)_{intf}$$

Where c(r,t) is the concentration field of the soluble element (here Ni) and R(t) denotes the evolution of precursor radius during its dissolution. D is the effective diffusion coefficient of Ni in the dealloying region. c_0 and c_{intf} denote respectively the concentrations in Ni of the precursor and at the dealloying interface, assumed to be fixed by a local equilibrium condition. Combined with a no-flux boundary condition at R_{intf}. This sharp-interface problem can be solved numerically using finite differences: time and space are discretized with Δx=0.01 µm and Δt= 10 µs finite steps and a forward Euler scheme is used for the time integration. To mimic experimental conditions, the following values are chosen for the parameters:

D= 0.2 10^{-9} $m.s^{-2}$. Effective diffusion coefficients in liquid metal are usually around D= 10^{-9} $m.s^{-2}$ [58]. However, to the best of our knowledge, there is no reported value for the Ni diffusion coefficient in an Mg melt so we used it as a varying parameter for the model to fit the experimental results. The fitted value has the same order of magnitude as a standard diffusion coefficient of atoms in a metallic melt, much higher than the diffusion coefficient of Ni in solid Mg (D= 10^{-15} $m.s^{-2}$). This lower obtained value can be explained by the presence of solid phase (FeCr ligaments) in the Mg liquid which is not considered in the model. It should also be noticed that this parameter does not change the overall shape of the curve but only the time required to perform dealloying.

c_intf is taken equal to 18%, corresponding to the maximum Ni solubility in a Mg bath measured by SEM-EDX after partial dealloying at a low dealloying temperature.

R_0 corresponds to the experimental size measured on the X-ray tomography reconstruction of our precursor sample.

R_intf is equal to 1000 µm corresponding to our quartz crucible radius.

3. Results

In this section we will analyze the dealloying and etching processes by both X-ray tomography and X-ray diffraction for one precursor composition with a high Ni content ($(FeCr)_{30}Ni_{70}$).

3.1. Dealloying process imaged by X-ray tomography

Fig. 1 shows 2D cross-sections extracted from a 3D reconstruction. It corresponds to raw images without further image treatment. The gray values are proportional to the material's absorption (linked to its atomic number), therefore air/vacuum and magnesium are dark-gray while the precursor tip is pale-gray. Due to the use of phase contrast imaging, a contrast between Mg and air can be observed even if their densities are much lower than Ni and Fe. The dealloyed part of the tip, a bi-phased microstructure rich in magnesium, is less attenuating than the precursor phase which contains nickel and it exhibits an intermediate gray value. The dealloyed front is therefore clearly visible. In the background, Mg flakes are visible around the precursor tip. Due to the shape of the Mg flakes, there is a lot of space between the flakes, but it is evident that there is enough magnesium around the tip and touching the precursor to allow the dealloying process to occur.

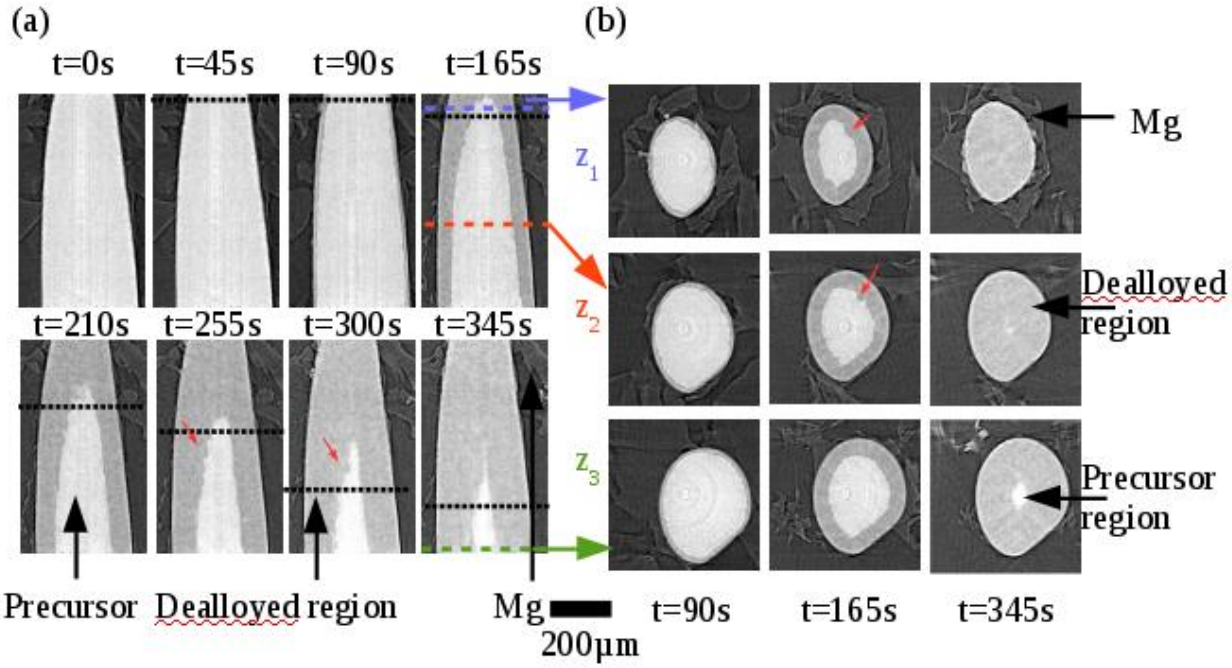

Fig. 1: Evolution of a dealloying front during the dealloying process from $(FeCr)_{30}Ni_{70}$ (a) sagittal slices of the sample at different intervals (b) 3 different horizontal slices at 3 intervals corresponding approximately to the position of the dashed colored line in (a). Black dashed lines correspond to the volume used to quantify the evolution of the dealloying process. Red arrows highlighted some irregularities noticed at the precursor/dealloying part boundaries.

Heating is started at t = 0 s from room temperature. Dealloying is not observed to occur before 45 s. From t = 90 s to t = 345 s, both precursor and dealloyed phases are visible. At t = 390 s (not shown in Fig. 1) the visible part of the sample is dealloyed completely. A first important observation is that the global shape of the sample remains almost unchanged (the volume change corresponds to around 1%, which is included in the error due to the threshold process) during the dealloying process, while the microstructure evolves strongly. For this sample, the dealloying process took approximately 5 mins to be completed, including an incubation time necessary to heat from room temperature. During the heating ramp, the sample moved slightly and acquisitions had to be stopped (between t = 90 s and t = 165 s) to allow us to re-center the sample. Even though the dealloying front moved during the acquisition, reconstructions at low magnification are not blurred, therefore reconstructions can be considered as an average state between the acquisition beginning and end. A systematic error is introduced by considering the reconstruction as the final state.

In the dealloyed area, FeCr ligaments cannot be resolved individually as they are smaller than the voxel. From results performed on Fe-Ni samples, ligament sizes around 0.8 µm are expected [8]. The spatial resolution of X-ray imaging detectors is often taken as two times the pixel size [60], leading in this case, to a value of 0.64 µm, which is too large to resolve the ligament microstructure. The irregularities of the dealloying front highlighted by red arrows, as observed in Fig. 1 (t = 165 s / z_1) for example, did not seem to be connected to the Mg flake distribution but are similar to observations of grain boundary positions as achieved by [10]. It was previously observed, that dealloying first affects grain boundaries [10]. This would suggest either a precursor with large grains or a cold-rolled precursor which underwent a first step of recrystallization before dealloying started, transforming the highly deformed cold-rolled microstructure into a partially recrystallized microstructure containing large grains [40]. Therefore, and from previous studies [40], it can be hypothesized that these irregularities are linked to the position of the grain boundaries.

For every reconstructed volume, dealloyed and precursor phases are segmented and phase thickness is measured using Fiji's "*local thickness*" function. As the tips are manually prepared, cross-sections are not perfectly circular and tip thickness is not constant along the length: tips are thinner on the top (see Fig. 1). To quantify the dealloying evolution, only the body part of the tips is used, far from the top, as illustrated in Fig 1 (part below the black dashed lines). From the phase thickness distribution, the 3D average dealloyed phase thickness can be extracted and is shown with black dots and labeled as 3D in Fig. 2. From Fig. 1, the 2D dealloying thickness for different heights (z_1, z_2, z_3) are manually measured by taking the average of around ten measurements and plotted in Fig. 2 (labeled as z_1, z_2, z_3). Error bars correspond to the standard deviation. At a given time the dealloying thickness along the tip appears rather constant, suggesting that in spite of the heterogeneity of the Mg flake distribution around the tip, the dealloying process occurs everywhere. Moreover, all experimental data are very close, validating the previous assumption that the dealloying rate is homogeneous in the whole sample height. Even if the dealloying rate is higher at grain boundaries, this difference is small enough to lead to an apparent homogeneous behavior. From Fig. 2, the calculated dealloying rate on the linear part is 0.42±0.03 µm/s and incubation time 61±3 s.
The observation of the dealloying front evolution of Au-Ag precursor by free corrosion on a cylindrical shaped precursor have been observed in [25]. These authors also demonstrated that the dealloying fron propagated homogeneously in three dimensions leading to the preservation of the sample morphology. The dealloying kinetic curves showed also a linear part. However, the rate was around 17 times lower, probably due to a very low temperature, compared to this experiment where the temperature was higher [25]. These results confirm similarities in mechanisms between liquid metal dealloying with conventional electrochemical dealloying.

The dealloying kinetics observed in Fig. 2 do not seem to follow a $t^{1/2}$ behavior characteristic of a diffusive process and previously observed in *post mortem* experiments [10, 35, 37]. When comparing these experiments however, the precursor shape is a major difference (a tip, not a plate) therefore diffusion occurs in all directions. To better understand the influence of the precursor shape, simulations are performed assuming a local equilibrium at the dealloying front and a dealloying kinetic limited by the diffusion of Ni in a cylindrical geometry with the data listed in section 2.6 and is plotted as a continuous line on Fig. 2. To perform this simulation, R_0 = 160 µm was measured from the X-ray tomography reconstruction. Experimentally, dealloying did not start before t=45s. However, for the simulation, dealloying started at t=0s. Therefore, to compare both results, 2 different axes are used: blue for the experimental data and black for the simulation. The qualitative agreement of the model to the experimental results is good. To match the results, the diffusion coefficient value is adjusted (D = 0.2 10^{-9} m/s). This low value can be explained by the presence of ligaments inside the bath which modifies the kinetics and are not considered in the model. The deviation from the square-root behavior characteristic of diffusion-limited kinetics can

be directly related to the sample morphology: the reduction of the dealloying front section during the dealloying process explains the acceleration of the dealloying rate at the end of reaction. Therefore, liquid dealloying kinetics are controlled by the Ni diffusion in the bath.

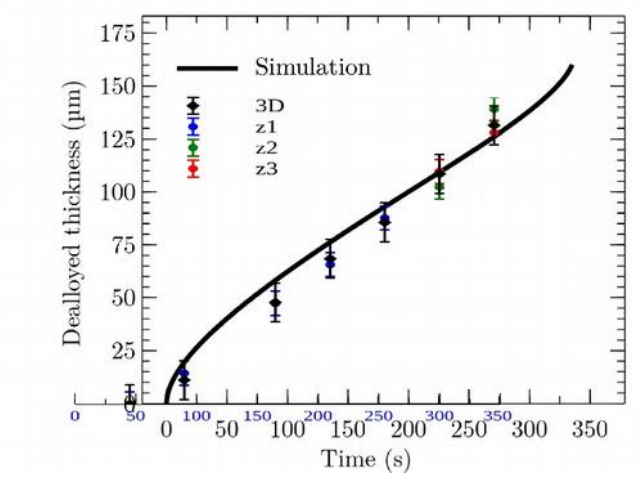

Fig. 2 Evolution of dealloying thickness with time for 2D and 3D measurements (blue axis). The continuous line corresponds to the simulation (black axis)

3.2 Dealloying process followed by X-ray diffraction (XRD)

XRD measurements give access to phase quantification and lattice parameters of the phases. The evolution of the different phases during the experiment was estimated by directly following the peak intensity or by following the evolution of the lattice parameter compared to a reference, expressed as an average strain: $\varepsilon = (d - d_0)/ d_0$ where d_0 is a selected reference state at room temperature here: first acquisition for the FCC precursor and last acquisition for the BCC dealloyed sample.

This is illustrated in Fig. 3, using the (111) and (200) peaks for the FCC precursor and the (110) and (200) peaks for the BCC dealloyed sample. The intensity of the different peaks is shown using dashed lines while the relative strains are plotted with continuous lines. In this case, following the dealloying steps means following a FCC-BCC phase transformation.

At the beginning, only FCC peaks are present because the precursor is entirely FCC. When heating starts, the relative strain increases because of thermal dilatation. From this curve, the sample temperature is evaluated to be around 938 K, which is consistent with the calibration performed prior to this experiment, with only the precursor tip (around 933 K).

At high temperature, the decrease in intensity for the FCC phase indicates the beginning of the dealloying process: the amount of the FCC phase decreases because the Ni dissolution induces a phase transformation. The newly created BCC phase is detected at around 25s (increasing BCC peak intensity).

However, the exact time when the two phases coexist is not detectable here as the signal to noise ratio is too low to be analyzed. This can be due to the fact that i) part of the precursor is replaced with the liquid (decrease of the diffracting volume) ii) atoms migrate at the dealloying front leading to a high disorder (loss of coherency) iii) crystallites are very small before coarsening (peak intensity spread due to nanosize effect).

If the sample is kept at high temperature, the microstructure coarsens, leading to an increase in ligament size. Because ligaments are single crystals, the grains grow along with the ligaments. This can explain the increase of the intensity (larger grain, less disorder). From phase diagrams [41-43] and previous studies [37, 39], it is known that after the phase transformation, the amount of Ni in the ligaments is still high, while the final amount is measured as null at the end of the experiment. Therefore, there is still Ni dissolution from the BCC phase which explains the shape of the relative strain curves during coarsening, exhibiting reduced cell size, until the remaining Ni in a solid solution diffuses towards Mg [62-64].

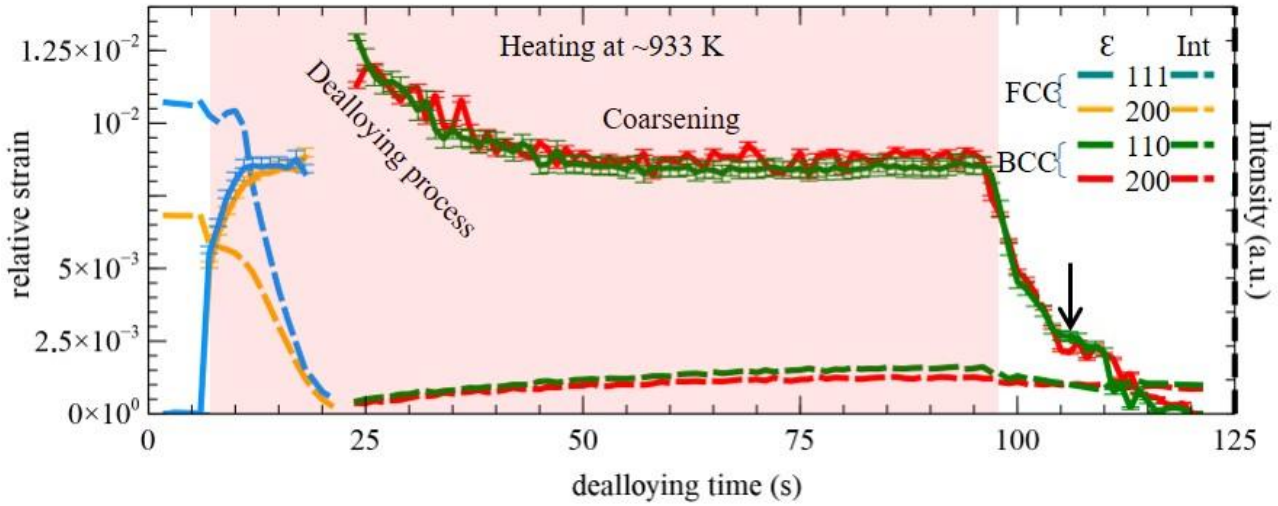

Fig. 3 Evolution of relative strain (continuous lines) and intensity (dashed lines) of 2 different FCC precursors and 2 different BCC dealloyed diffraction peaks during dealloying. The arrows highlight interaction between the 2 phases during the cooling step.

Literature indicates that the FeCr phase ($\alpha Fe_{75}Cr_{25}$ = 11.7 10^{-6} /K at 600 K) has a lower linear dilatation coefficient than the Mg phase ($\alpha Mg_{95}Ni_5$ = 29.7 10^{-6} /K at 600 K) [66]. At dealloying temperature, Mg is liquid so both phases are in equilibrium. The shape of the strain evolution during cooling is mostly due to the temperature change. At the end of cooling, when the magnesium solidifies, the curves become disrupted due to both temperature cooling and possible incompatibility strains building between both interconnected solid metals with two different dilation coefficients. This point is highlighted by an arrow in Fig. 3. By extrapolating the relative strain slope before phase interactions (around from 95 s to 105 s) during cooling until the 125 s mark, we can estimate the relative strain without thermal residual strain. Then, by subtracting the relative strain without thermal residual strain and the experimentally measured relative strain, the residual thermal strains are estimated between 0.1% and 0.2%. Taking into account the difference in the mechanical properties, the first material, which will present a plastic deformation, is expected to be the Mg phase (the yield strength of pure Mg is about 190 MPa, however the Ni in a solid solution may increase this value [65]). Therefore, while taking FeCr Young's modulus value as 210 GPa and considering the differing thermal expansion coefficient, the maximum residual elastic strain inside FeCr is evaluated to be 0.09%, which is consistent with the measured one.

3.3 Etching process imaged by X-ray tomography

To image the etching step of a dealloyed sample using X-ray tomography, a coarsened microstructure is necessary. For this reason, we use a sample dealloyed in the laboratory for 1 hr at 1093 K from a $(FeCr)_{30}Ni_{70}$ precursor.

Fig. 4(a) presents a 2D slice extracted from a 3D reconstruction after t = 1048 s of etching. Both phases are present: FeCr ligaments (bright) and Mg phase (dark gray). The red ellipse highlights either a microstructural defect such as a precursor grain boundary position, or a defect introduced during the sample preparation prior to the etching process. In this case, this microstructural defect corresponds to a crack due to sample preparation. As mentioned in a previous study, the propagation of the dissolution front is perpendicular to the reaction interface [16]. Chemical etching is performed in the whole bulk sample. Fig. 4(b) shows the evolution of FeCr ligaments and the second phase Mg/air phase thickness during the etching step, measured on a cube of about 100 µm, taken in the center of the tip corresponding to a representative elementary volume taken in a "defect-free" area. At the beginning of the experiment, the second phase corresponds to Mg and during etching it corresponds to a mix of etchant and Mg. At the end, when etching is completed, the second phase corresponds to aqueous liquid only. Both systems present unimodal distribution

which is similar to previous studies [40, 67, 68]. The average FeCr ligament size is estimated to be 4.5 ± 0.5 µm similar to that measured in [40] and is constant during the process. On the contrary, the average thickness of the Mg/etchant phase increases from 5.5 µm to more than 6.7 µm. The final pore size is consistent with that measured in [40]. This shift in the average thickness of Mg/air, means that the space between ligaments becomes larger when the etching step occurs. The FeCr phase volume ratio decreases (cf. the inset of Fig. 4(b)) during the process and indicates that the sample expands. It can be noticed that this expansion is greater locally, where the sample presents defects.

From Fig. 4(a) and all reconstructions, the evolution of the etching front can be measured manually by taking the average of around five Mg phase thickness measurements. The evolution of the etching front is linear with time and can be evaluated to be roughly equal to 20 nm/s (corresponding to an evolution of around 8 voxels for each acquisition) which is quite low to compare with the 130 s of acquisition time. This very low etching rate can be increased by increasing nitric acid concentration [7].

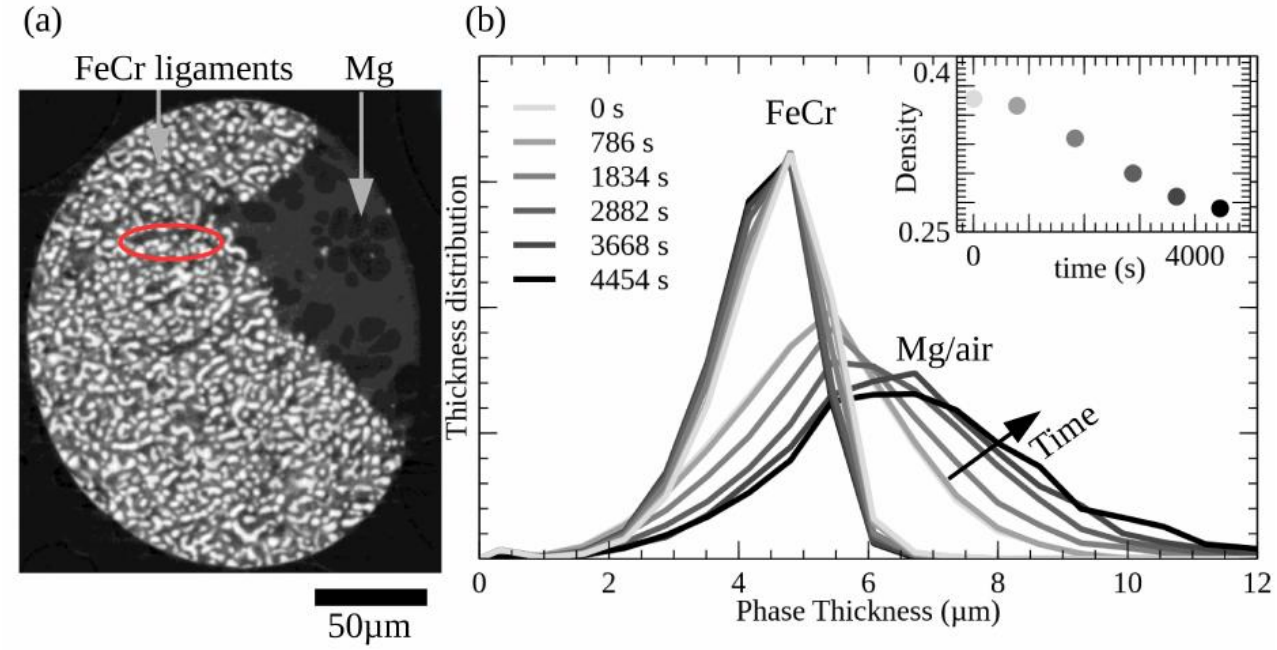

Fig. 4(a) 2D view extracted from a 3D reconstruction for t = 1048 s. The red ellipse highlights a defect (b) Evolution of FeCr and Mg/air-etchant phase thickness during the sacrificial phase etching step. As inset, the evolution of the FeCr phase volume ratio (relative density) is plotted.

As mentioned in the previous section, after the cooling process, the FeCr phase is under compression. The suggested lattice strain estimated in the previous section is very small so it cannot be detected in the images visually. However, this global expansion (except peeling) is not observed for bulk samples [40]. Before the X-ray tomography experiment, 1 mm side square samples are polished to obtain a <300 µm diameter tip. Therefore, one can imagine that mechanical stresses are accumulated during this preparation. The stress releases observed here denotes the relaxation of mechanical stresses leading to peeling formation due to the cold-rolling step of the precursor sample [69].

Previous studies on dealloyed TiCrZr-Mg to give porous TiCrZr after Mg etching, also showed that TiCrZr ligament sizes were almost not affected by the etching step (slight increase) [38]. However, these authors calculated a smaller pore thickness than that using Mg ligaments. The difference between these two results can be explained by different measuring techniques: in this study, pore size was measured while in [38], pore size was calculated as the ratio between the volume and surface area.

3. 4 Etching process followed by X-ray diffraction

The etching step is also followed by X-ray diffraction. The reference state (d_0) is taken at room temperature prior to the etching solution immersion. Fig. 5 shows the XRD diffraction pattern after chemical etching and the evolution of the relative lattice parameters of the dealloyed phase for 30%FeCr and 70%FeCr samples in red and gray respectively. The acquisition for the 70%FeCr XRD experiment is very noisy due to large grains, implying a more erratic diffraction signal. Despite the very noisy data, two steps can be distinguished. On the first step, up to around 500 s, the lattice parameters are stable because enough Mg should be removed before stress relaxation. A first part, where the Mg/air average thickness is stable, has already been noticed in the previous section. Then the lattice parameters increase by 0.15%. Examining a stainless steel with E = 210 GPa, this strain is equivalent to 315 MPa of residual stress relaxation. A relative strain relaxation of 0.15 % is in good agreement compared to the strains created during the cooling step (estimated between 0.1 and 0.2%).

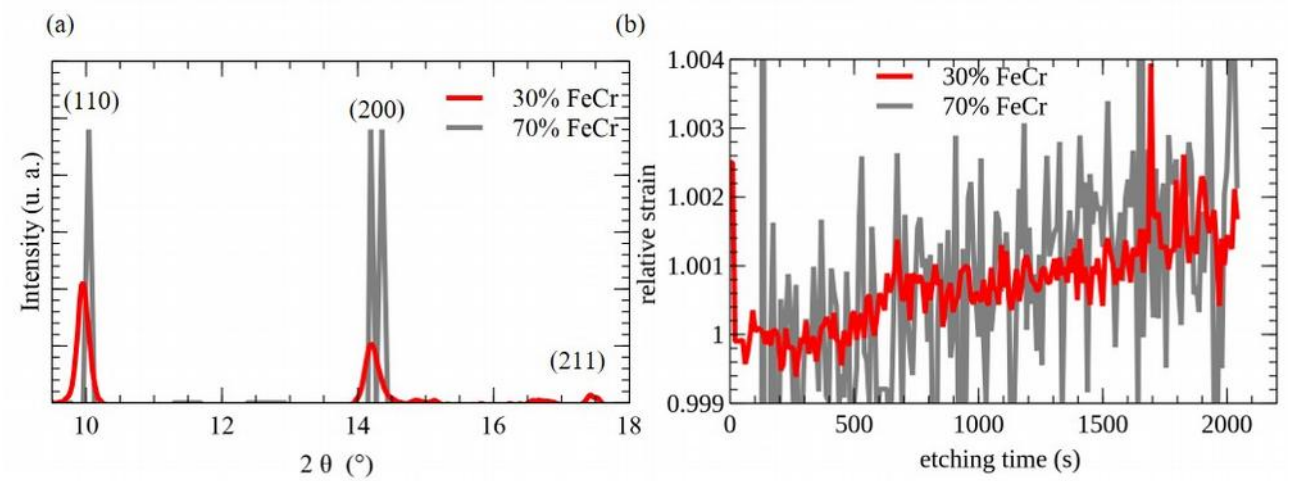

Fig. 5 (a) XRD diffraction pattern after chemical etching (t=1700s) (b) Evolution of the relative lattice parameter during the Mg phase etching of 30%FeCr (red) and 70%FeCr samples (gray).

4. Discussion

In the previous section, we analyzed the dealloying and etching behavior of a $(FeCr)_{30}Ni_{70}$ precursor. The same procedure is used for analyzing all different precursor compositions and in this section, we will discuss the influence of the Ni content in the precursor on the dealloying and etching behavior by comparing experiments carried out using $(FeCr)_{30}Ni_{70}$ and $(FeCr)_{70}Ni_{30}$ precursors.

4.1 Discussion on the influence of precursor composition on the etching process

Whereas the strain evolution during the etching process seems similar for different precursor composition (cf. Fig. 5), the acquisition for 70%FeCr XRD experiment is very noisy due to large grains implying lower diffraction signal, therefore it is difficult to discuss the detailed behavior. However, the stress relaxation level seems independent of the initial FeCr/Mg phase ratio.

Contrary to the similarities noticed by X-ray diffraction, a different behavior depending on precursor composition is observed with the X-ray tomography data. For both samples, the etching front is perpendicular to the reaction interface, however the expansion observed for 30%FeCr is not detectable for 70%FeCr as shown in appendix 3. For the 70%FeCr sample, the FeCr phase thickness, Mg/etchant phase thickness and phase ratio are preserved during the etching process. The preservation of the 70%FeCr shape is probably due to the higher amount of FeCr and a stronger FeCr phase connectivity [40].

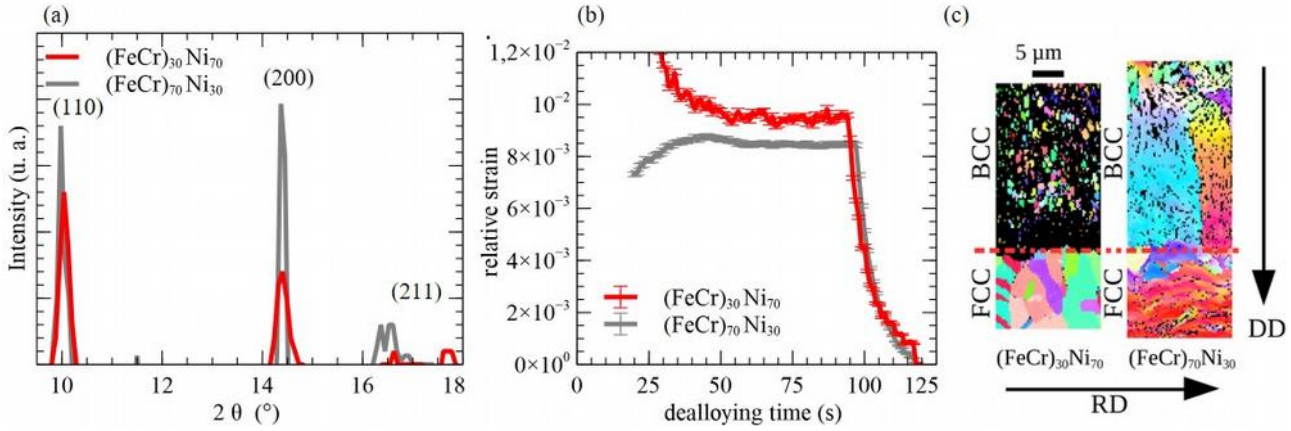

Fig. 6 (a) XRD diffraction pattern of the BCC phase (t=80s) (b) Evolution of relative strain and of BCC dealloyed diffraction peaks (111) during dealloying of a $(FeCr)_{30}Ni_{70}$ (red) and $(FeCr)_{70}Ni_{30}$ (gray) precursors (c) IQ+IPF SEM-EBSD map after 3 mins dealloying at 933 K from $(FeCr)_{30}Ni_{70}$ (left) and $(FeCr)_{70}Ni_{30}$ (right). The bottom part corresponds to the precursor and the top part to dealloyed portion. Arrows correspond to the cold-rolling direction (RD) and dealloying reaction direction (DD).

4.2. Discussion on the influence of precursor composition on the dealloying process

However, the use of two different heaters to perform dealloying *in situ* leads to a different temperature gradient/temperature that leads to different dealloying kinetics. For this reason, the results obtained from X-ray tomography and X-ray diffraction cannot be directly compared to each other.

Considering the X-ray tomography data, the effect of the amount of the Mg near the sample have been investigated with the simulation tool, by changing the R_intf. If the R_intf decreases, dealloying still occurs. The dealloying kinetics, however, are decreased. If different kinetics are observed between 2 differently composed samples and we are not able to de-correlate the influence of the precursor composition with the amount of Mg, then we are not able to discuss the influence of precursor composition on dealloying kinetics.

However, for all samples (other samples are shown in appendix 2 and 3), the dealloying front kinetic is homogeneous within the sample and the tip shape is preserved during the process. The curve of the evolution of dealloying thickness with time also shows a linear section and presents a good agreement with simulation.

On the other hand, the result obtained by diffraction can be analyzed depending on precursor compositions. Fig. 6(a) displays the evolution of the strain of the dealloyed phase for $(FeCr)_{30}Ni_{70}$ and $(FeCr)_{70}Ni_{30}$ precursors, with red and gray lines analyzed on the (111) peak respectively. The choice of the value of d_0 in the strain calculation is always crucial. We chose this reference as the value of d_0 at room temperature, which explains why the strains are identical in the two samples after dealloying and cooling down to room temperature. And the different strain level at high temperature before cooling can possibly be due to a slight variation in the dealloying temperature in these two different experiments. We estimated that a temperature difference of about 60 K could explain the observed strain difference.

While the strain decreases at the beginning of the coarsening step of a dealloyed sample from $(FeCr)_{30}Ni_{70}$ precursor, the stain increases for the dealloyed sample from $(FeCr)_{70}Ni_{30}$ precursor which is not consistent with a Ni dissolution from the BCC phase, which leads to a reduction in cell size. Moreover, in our previous studies [40, 70] *post mortem* XRD acquisition and EBSD maps also show a difference, especially on the dealloyed grain microstructure between $(FeCr)_{70}Ni_{30}$ and

$(FeCr)_{30}Ni_{70}$ precursor samples. To explain the difference observed between the two samples (cf. Fig 6(a)), partial dealloying is performed to directly observe the dealloyed grain formation.
Fig. 6(b) presents the grain microstructure after dealloying for 3 mins at 933 K with Index Quality (IQ) + Inverse Pole Figure (IPF) maps. The top part corresponds to the dealloyed area and the bottom part to the precursor area. Arrows correspond to the cold-rolling direction (RD) and dealloying reaction direction (DD), respectively. The precursor portion is totally recrystallized for the $(FeCr)_{30}Ni_{70}$ precursor while we observe a partial recrystallization only for the $(FeCr)_{70}Ni_{30}$ precursor. The dealloying thickness layers (only partially shown here) are also different: 240 µm for the $(FeCr)_{30}Ni_{70}$ precursor versus 50 µm for the $(FeCr)_{70}Ni_{30}$ precursor. The main difference comes from the microstructure: the dealloyed area from the $(FeCr)_{30}Ni_{70}$ precursor presents small grains composed of a couple of ligaments which look randomly oriented while large grains including many ligaments are visible in the dealloyed area from the $(FeCr)_{70}Ni_{30}$ precursor. This columnar grain suggests an epitaxial grain growth with a grain growth orientation competition [71] which can imply the tensile strain observed on Fig. 6(a) for a dealloying time less than 50s. Usually, for the FCC/BCC system, the <100>direction is the dominant one. However our card is not large enough to be able to make a conclusion about favorite directions [72,73]. From literature, it seems that the large grains observed after dealloying from $(FeCr)_{70}Ni_{30}$ precursors suggests that their orientation is not linked with the precursor grain orientation. In opposition, the smaller grains observed after dealloying from $(FeCr)_{30}Ni_{70}$ precursors, compared to the precursor grains, suggest that the precursor and dealloyed grains could have some orientation relationships corresponding to a diffusionless phase transformation [74, 75].

4.3. Summary of the suggested scenario

Fig. 6 thus highlights the different dealloyed grain transformation mechanisms. We compile all differences between the two samples and explain the different grain formation mechanisms in a schematic in Fig. 7.
If one considers the same interface precursor/dealloyed sample, when the amount of FeCr is low (i.e. $(FeCr)_{30}Ni_{70}$ precursor), the dealloying front reaction moves quickly, which promotes diffusion with the formation of FCC ligaments followed (ligaments in red color) by a displacive transformation to form BCC ligaments leading to a decrease in lattice parameters (Fig. 6(a)). As a consequence, the nucleation of new grains is easier (cf. Fig. 7(a)). However, when the amount of FeCr is high (i.e. $(FeCr)_{70}Ni_{30}$ precursor), the dealloying front reaction moves slowly. Due to their high quantity, Fe and Cr atoms are closer to each other and due to the low dealloying rate, Ni has time to diffuse in Mg, therefore it is easier to have a diffusive phase transformation with the direct formation of BCC ligaments, leading to an epitaxial grain growth rather than nucleation of new grains (cf. Fig. 7(b)). This ultimately leads to an increase in the relative strain (cf. Fig. 6(a)) [71,74].

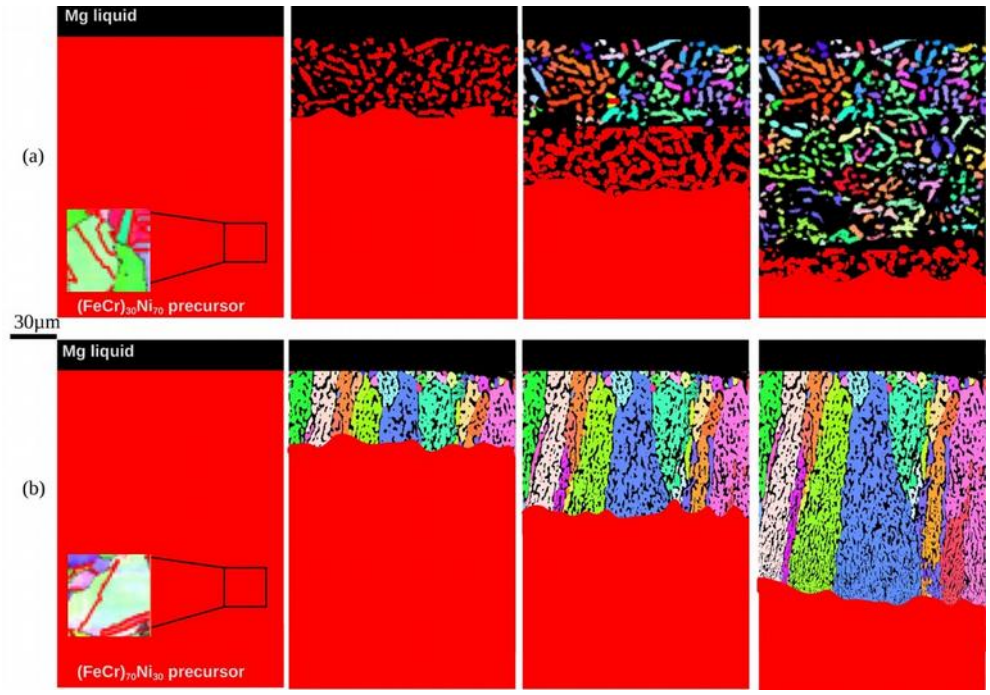

Fig. 7 Grain formation during dealloying. The red part corresponds to the FCC phase. (a) for a low amount of FeCr, the high kinetics of dealloying promotes a morphological transformation with the formation of FCC ligaments followed by a displacive transformation, (b) for a high amount of FeCr, the slow kinetics of dealloying promotes a diffusive transformation with the direct formation of BCC ligaments

5. Conclusion

Porous FeCr is prepared *in situ* using liquid metal dealloying by immersing $(FeCr)_{30}Ni_{70}$ and $(FeCr)_{70}Ni_{30}$ precursors into a Mg metallic melt bath to create a FeCr-Mg rich bicontinuous structure, then the Mg rich phase is chemically etched.

This entire process is analyzed by X-ray tomography and X-ray diffraction measurements.

For a $(FeCr)_{30}Ni_{70}$ cylindrical shape precursor, the dealloying kinetics present a large linear section with a dealloying rate of about 0.42±0.03 µm/s constant in the three directions. The morphology of the sample shape is preserved during the dealloying step. Using a phase field model and accounting for the cylindrical sample shape, it is possible to simulate the evolution of the dealloying front. The consistence between experimental and simulated values proves that the process is controlled by the diffusion of Ni in the Mg bath.

XRD measurements show different behavior depending on precursor composition. For a low amount of FeCr at the early stage of coarsening, a slight decrease in the lattice parameter of the BCC phase is observed, while for a sample with a high amount of FeCr, an increase in the lattice parameter is observed. This difference is clarified by the dealloyed grain formation mechanism. On the one hand, in the case of a low FeCr/Ni ratio in the precursor, a displacive transformation occurs, with new grain nucleation leading to the decrease in the crystal lattice when the remaining Ni atoms leave the crystal lattice. On the other hand, in the case of a large FeCr/Ni ratio in the precursor, we observed a diffusive phase transformation with an epitaxial growth leading to tensile stress.

During cooling, the interaction of ligaments and the Mg phase is noticeable. This interaction creates a large residual thermal strain due to the different thermal dilation coefficients and this thermal strain is relaxed during the etching step.

This paper shows the feasibility of *in situ* observations during the dealloying and etching process with a qualitative analysis with an appropriate set-up. As a perspective, the set-up can be improved to have a better control of temperature and the amount of Mg around the precursor tip, to evaluate

the influence of more parameters like precursor composition/preparation or the dealloying temperature on dealloying kinetics.

Acknowledgement
This work was supported by Région Rhone-Alpes, Erasmus+ program and the French ministry of research. We acknowledge the Paul Scherrer Institut, Villigen, Switzerland for provision of synchrotron radiation beamtime at beamline TOMCAT of the SLS and European Synchrotron Radiation Facility, Grenoble, France for provision of synchrotron radiation beamtime at beamline ID11. Authors acknowledge François Cadiou and Julie Devillard for their help during synchrotron experiments, Kader Benaziza for manufacturing sample holders and Tomcat and ID11 beamline staff.

Declaration of competing interest
The authors have no conflicts of interest to declare.

Appendix 1: Illustration of experimental set-up

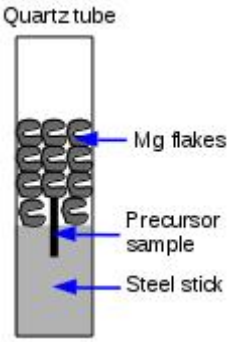

Appendix 2: Sagittal slices extracted from the 3D reconstruction showing the evolution of dealloying front during dealloying process from $(FeCr)_{70}Ni_{30}$ precursor sample. Light gray and median gray correspond respectively to precursor area and to dealloyed area.

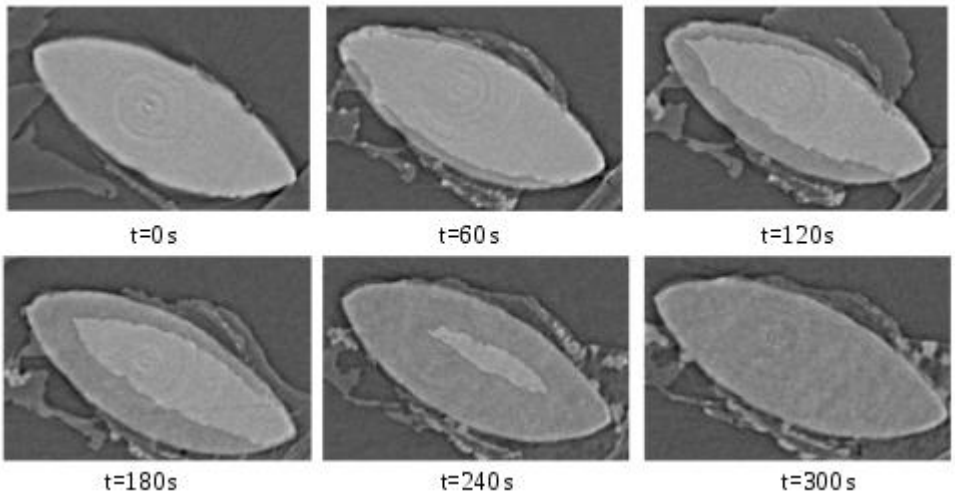

Appendix 3: (a) Evolution of dealloying thickness with time from $(FeCr)_{70}Ni_{30}$ precursor sample. To be able to compare simulation and experimental values, the experimental incubation time was subtracted from the experimental time. The continuous line corresponds to the simulation. (b) Evolution of FeCr and Mg/air phase thickness during sacrificial phase etching step of a dealloyed sample from a $(FeCr)_{70}Ni_{30}$ precursor.

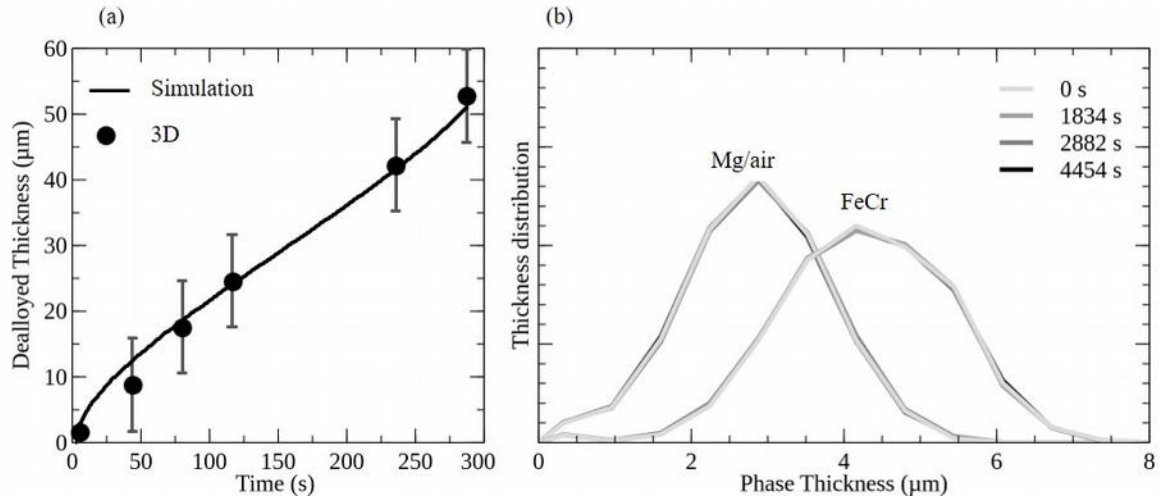

References

[1] J. Erlebacher, R.Seshadri, Hard materials with tunable porosity, MRS Bull 34 (2009) 561–568.

[2] J. Snyder, T. Fujita, M. Chen, J. Erlebacher, Oxygen reduction in nanoporous metal–ionic liquid composite electrocatalysts, Nat. Mater. 9 (2010) 904-907.

[3] X.Y. Lang, A. Hirata, T. Fujita, M. Chen, Nanoporous metal/oxide hybrid electrodes for electrochemical supercapacitors, Nat. Nanotechnol. 6 (2011) 232-236.

[4] S. Chen, Y. Chu, J. Zheng, Z. Li, Study on the two dealloying modes in the electrooxidation of Au–Sn alloys by in situ Raman spectroscopy, Electrochimica Acta 54 (2009) 1102–1108.

[5] K. Sivula, R. Zboril, F.L. Formal, R. Robert, A. Weidenkaff, J. Tucek, J. Frydrych, M. Grätzel,Photoelectrochemical Water Splitting with Mesoporous Hematite Prepared by a Solution-Based Colloidal Approach., J. Am. Chem. Soc., 137 (2010) 7436-7444.

[6] M. Hakamada, M. Takahashi, T. Yamamoto, J. Motomura, M. Mabuchi, Less noble nanoporous metals fabricated by dealloying, in: Abstract Book of the seventh International Conference on Porous Metal and Metallic Foam, MetFoam2011, 69-69.

[7] T. Wada, K. Yubuta, A. Inoue, H. Kato, Dealloying by metallic melt, Mater. Lett. 65 (2011) 1076-1078.

[8] T. Wada, H. Kato, Three-dimensional open-cell macroporous iron, chromium and ferritic stainless steel, Scr. Mater. 68 (2013) 723-726.

[9] J.W. Kim, T. Wada, S.G. Kim, H. Kato, Sub-Micron Porous Niobium Solid Electrolytic Capacitor Prepared by Dealloying in a Metallic Melt, Mater. Lett.116 (2014) 223-226.

[10] I. McCue, B. Gaskey, P.-A. Geslin, A. Karma, J. Erlebacher, Kinetics and morphological evolution of liquid metal dealloying, Acta Mater. 115 (2016) 10-23.

[11] I. V. Okulov, S. V. Lamaka, T. Wada, K. Yubuta, M. L. Zheludkevich, J. Weissmuller, J. Markmann, H. Kato, Nanoporous magnesium. Nano Res. 11 (2018) 6428–6435.

[12] T. Wada, A. D. Setyawan, K. Yubuta, H. Kato, Nano- to submicro-porous b-Ti alloy prepared from dealloying in a metallic melt, Scr. Mater. 65 (2011), 532-535.

[13] I. V. Okulov., J. Weissmuller, J. Markmann, Dealloying-based interpenetrating-phase nanocomposites matching the elastic behavior of human bone. Sci. Rep. 7(20) (2017) 77-87.

[14] A. Okulov, A. Volegov, J. Weissmuller, J. Markmann, I. Okulov, Dealloying-based metal-polymer composites for biomedical applications. Scr. Mater. 146 (2018) 290-294.

[15] I. Okulov, A. Okulov, I. Soldatov, B. Luthringer, R. Willumeit-Romer, T. Wada, H. Kato, J. Weissmuller, J. Markmann, Open porous dealloying-based biomaterials as a novel biomaterial platform. MSE C 88 (2018) 95-103.
[16] M. Mokhtari, C. Le Bourlot, J. Adrien, S. Dancette, T. Wada, J. Duchet-Rumeau, H. Kato, E. Maire, Cold-rolling influence on microstructure and mechanical properties of NiCr-Ag composites and porous NiCr obtained by liquid metal dealloying, J. Alloys Compd., 707, (2017), 251–256.
[17] M. Mokhtari, T. Wada, C. Le Bourlot, N. Mary, J. Duchet-Rumeau, H. Kato, E. Maire,
Low cost high specific surface architectured nanoporous metal with corrosion resistance produced by liquid metal dealloying from commercial nickel superalloy, Scr. Mater. 163 (2019) 5-8.
[18] M. Mokhtari, T. Wada, C. Le Bourlot, J. Duchet-Rumeau, H. Kato, E. Maire, N. Mary,
Corrosion resistance of porous ferritic stainless steel produced by liquid metal dealloying of Incoloy 800, Corros Sci. (2020) 108468.
[19] T. Wada, T. Ichitsubo, K. Yubuta, H. Segawa, H. Yoshida, H. Kato, Bulk-Nanoporous-Silicon Negative Electrode with Extremely High Cyclability for Lithium-Ion Batteries Prepared Using a Top-Down Process, Nano Lett.,14 (8) (2014) 4505–4510.
[20] S.G. Yu, K. Yubuta, T. Wada, H. Kato,Three-dimensional bicontinuous porous graphite gerenated in low teperature metallic melt, Carbon 96 (2016) 403-410.
[21] Y. Zhao, X. Wang, J.C. Huang, X. Chen, L. Cao, M. Mu, Affection of Cu content on the phase evolution during the dealloying of Ag-Cu alloys using electrochemical noise with Hilbert spectra analysis Materials Letters 183 (2016) 165–169.
[22] P. Rajput, A. Gupta, B. Detlefs, D. M. Kolb, S. Potdar, J. Zegenhagen, Dealloying of Cux Au studied by hard X-ray photoelectron spectroscopy, Journal of Electron Spectroscopy and Related Phenomena 190 (2013) 289–294.
[23] R. Srivastava, P. Mani, P. Strasser, In situ voltammetric de-alloying of fuel cell catalyst electrode layer: A combined scanning electron microscope/electron probe micro-analysis study, Journal of Power Sources 190 (2009) 40–47.
[24]Y.-C. K. Chen-Wiegart, S. Wang, Y. S. Chu, W. Liu, I. McNulty, P. W. Voorhees, D. C. Dunand, Structural evolution of nanoporous gold during thermal coarsening, Acta Mater. 60 (2012) 4972–4981.
[25] Y.-C. K. Chen-Wiegart, S. Wang, W.-K. Lee, I. McNulty, P. W. Voorhees, D. C. Dunand, In situ imaging of dealloying during nanoporous gold formation by transmission X-ray microscopy, Acta Mater. 61 (2013) 1118–1125.
[26]Y.-C. K. Chen-Wiegart, S. Wang, I. McNulty, D. C. Dunand, Effect of Ag–Au composition and acid concentration on dealloying front velocity and cracking during nanoporous gold formation, Acta Materialia 61 (2013) 5561–5570.
[27] J. Zegenhagen, F.U. Renner, A. Reitzle, T.-L. Lee, S. Warren, A. Stierle, H. Dosch,
G. Scherb, B.O. Fimland, D.M. Kolb, In situ X-ray analysis of solid/electrolyte interfaces: electrodeposition of Cu and Co on Si(1 1 1):H and GaAs(0 0 1) and corrosion of Cu_3Au(1 1 1), Surf. Sci. 573 (2004) 67-79.
[28] F.U. Renner, A. Stierle, H. Dosch, D.M. Kolb, T.-L. Lee, J. Zegenhagen, Initial corrosion observed on the atomic scale, Nature 439 (2006) 707-710.
[29]F.U. Renner, Y. Gründer, P.F. Lyman, J. Zegenhagen, *In-situ* X-ray diffraction study of the initial dealloying of Cu_3Au(001) and $Cu_{0.83}Pd_{0.17}$(001), Thin Solid Films 515 (2007) 5574-5580.
[30] F.U. Renner, A. Stierle, H. Dosch, D.M. Kolb, T.L. Lee, J. Zegenhagen, In situ x-ray diffraction study of the initial dealloying and passivation of Cu3 Au(111) during anodic dissolution, Phys. Rev. B 77 (2008) 235433.
[31] S. Van Petegem, S. Brandstetter, R. Maass, A. M. Hodge, B. S. El-Dasher, J. Biener, B. Schmitt, C. Borca and H. Van Swygenhoven,On the Microstructure of Nanoporous Gold: An X-ray Diffraction Study Nano Lett., Vol. 9, No. 3, (2009) 1158-1163.
[32] C. Mahr, K. Müller-Caspary, M. Graf, A. Lackmann, T. Grieb, M. Schowalter, F. F. Krause, T. Mehrtens, A. Wittstock, J. Weissmüller, A. Rosenauer, Measurement of local crystal lattice strain variations in dealloyed nanoporous gold, Mater. Res 6(1) (2017) 84-92.

[33] Y. C. K. Chen-Wiegart, R. Harder, D. C. Dunand, I. McNulty, Evolution of dealloying induced strain in nanoporous gold crystals, Nanoscale 9(17) (2017) 5686-5693.
[34] P.-A. Geslin, I. McCue, B. Gaskey, J. Erlebacher, A. Karma,Topology-generating interfacial pattern formation during liquid metal dealloying, Nat. Commun. 6 (2015) 8887
[35] M. Tsuda, T. Wada, H. Kato, Kinetics of formation and coarsening of nanoporous α-titanium dealloyed with Mg melt, J. of Apl. Phy. 114 (2013) 113503.
[36] J. W. Kim, M. Tsuda, T. Wada, K. Yubuta, S. G. Kim, H. Kato. Optimizing niobium dealloying with metallic melt to fabricate porous structure for electrolytic capacitors, Acta Mater.,84 (2015) 497-505.
[37] T. Wada, K. Yubuta, H. Kato, Evolution of a bicontinuous nanostructure via a solid-state interfacial dealloying reaction, Scripta Mater. 118 (2016) 33–36.
[38] Y.-C. K. Chen-Wiegart, T. Wada, N. Butakov, X. Xiao, F. De Carlo, H. Kato, J. Wang, D. C. Dunand, E. Maire, 3D morphological evolution of porous titanium by x-ray micro- and nano-tomography, J. Mater. Res. 28 (2013) 2444-2452.
[39] C. Zhao, T. Wada, V. De Andrade, G. J. Williams, J. Gelb, L. Li, J. Thieme, H. Kato, Y.-C. K. Chen-Wiegart, Three-Dimensional Morphological and Chemical Evolution of Nanoporous Stainless Steel by Liquid Metal Dealloying ACS Appl. Mater. Interfaces *9* (39) (2017) 34172-34184.
[40] M. Mokhtari, C. Le Bourlot, J. Adrien, A. Bonnin, T. Wada, J. Duchet-Rumeau, H. Kato, E. Maire, Microstructure Characterization by X-ray tomography and EBSD of porous FeCr produced by liquid metal dealloying, Mater. Charac. 144 (2018) 166-172.
[41] J.S. Marsh Limits of New Phase in the Fe-Cr-Ni system, Met. Prog. 35 (1939) 269-272.
[42] F. H. Hayes, M. G. Hetherington, R. D. Longbottom, Thermodynamics of stainless steels, Mater. Dci. Technol. 6 (1990) 263-272.
[43] J.W. Pugh, J.D. Nisbet, Iron-chromium-nickel ternary system, Transactions AIME 188 (1950) 268-276.
[44] T. B. Massalski, H. Okamoto, P.R. Subramanian, L. Kacprzak, Fe-Cr phase diagram, Binary alloy phase diagrams, ASMI (2) (1990) 1273.
[45] I.V. Okulov, P.-A. Geslin, I.V. Soldatov, H. Ovri, S.-H. Joo, H. Kato, Anomalously low modulus of the interpenetrating-phase composite of Fe and Mg obtained by liquid metal dealloying, Scr. Mater. 63 (2019) 133-136.
[46] G. Voss, Die Legierungen: Nickel-Zinn, Nickel-Blei, Nickel-Thallium, Nickel-Wismut, Nickel-Chrom, Nickel-Magnesium, Nickel-Zink und Nickel-Cadmium, Z. Anorg. Chem.(1908)
[47] M.E. Straumanis, The Precision Determination of Lattice Constants by the Powder and Rotating Crystal Methods and Applications, J. Appl. Phys. 20 (1949) 726-734.
[48] D. Noréus, P.E. Werner, Structural Studies of Hexagonal Mg_2NiH_X, Acta Chem. Scand. A 36 (1982) 847-851.
[49] D. Paganin, S. C. Mayo, T. E. Gureyev, P. R. Miller, S. W. Wilkins, Simultaneous phase and amplitude extraction from a single defocused image of a homogeneous object, J. of Microscopy 206 (2002) 33-40.
[50]C. Hintermüller, F. Marone, A. Isenegger, M. Stampanoni, Image processing pipeline for synchrotron-radiation-based tomographic microscopy, J. Synchrotron Rad., 17 (2010) 550-559.
[51] F. Marone, B. Münch, M. Stampanoni, Fast reconstruction algorithm dealing with tomography artifacts, Proc. SPIE 7804, Dev. X-Ray Tomogr. VII (2010) 780410.
[52] F. Marone, M. Stampanoni, Regridding reconstruction algorithm for real time tomographic imaging, J. Synchrotron Rad. 19 (2012), 1029-1037.
[53] J. Schindelin, I. Arganda-Carreras, E. Frise et al., Fiji: an open-source platform for biological-image analysis, Nat. methods 9 (2012) 676-682.
[54] J. L. Fife, M. Rappaz, M. Pistone, T. Celcer, G. Mikuljan, M. Stampanoni, Development of a laser-based heating system for in situ synchrotron-based X-ray tomographic microscopy, J. Synchrotron Rad., 19, (2012) 352-358.
[55] J. Kieffer and D. Karkoulis, PyFAI, a versatile library for azimuthal regrouping, J. Phys.: Conf. Ser. 425 (2013) 202012-202017.

[56] J. Kieffer and J. Wright, PyFAI: A Python library for high performance azimuthal integration on GPU, Powder Diffraction *28*(S2) (2013) S339-S350.
[57] I. Groma, X-ray line broadening due to an inhomogeneous dislocation distribution, PRL 57(13) (1998) 7535-7542.
[58] E. Frohberg, K. H. Kraatz, H. Wever, A. Lodding, H. Odelius Diffusion in liquid alloys under microgravity DIMETA 88 (1990) 295-300.
[59] L. V. Pavlinov, A. M. Gladyshev, V. N. Bykov, Self-Diffusion in Calcium and Diffuse of Barely Soluble Impurities in Magnesium and Calcium,Phys. Met. Metall. 26(5) (1968) 53-59.
[60] *E. Maire, P. J. Withers, Quantitative X-ray tomography, Int. Mat. Rev. 59 (2014) 1-43*
[61] T. Hildebrand, P. Ruesgsegger, A new method for the model-independent assessment of thickness in three-dimensional images, J. of Microscopy 185 (1996) 67-75.
[62] V.D. Doroeolskii, S.M. Karalnuk, A.V. Koval, Solid solutions in the V-Ti, V-Fe, Fe-Cr and Fe-Ni systems, Metallofizika 41 (1972) 73-77.
[63] D.J. Dyson, B. Holmes, Effect of alloying additions on the lattice parameter of austenite, J. Iron Steel Inst. 208(1970) 469–474.
[64] R. Mohammadzadeh, M. Mohammadzadeh, Correlation between stacking fault energy and lattice parameter in nanocrystalline Fe–Cr–Ni austenitic stainless steels by atomistic simulation study, Int. J. Model. Simul. 37(4) (2017) 227-233.
[65] Tables of physical and chemical constants, Kaye and Laby, National physic library, www.kayelaby.npl.co.uk
[66] Y.S Touloukian, Thermophysical Properties of Matter, Vol. 12, Thermal Expansion, IFI/Plenum, New York, 1975.
[67] W.B. Liu, S.C. Zhang, N. Li, J.W. Zheng, S.S. An, Y.L. Xing, A general dealloying strategy to nanoporous intermetallics, nanoporous metals with bimodal, and unimodal pore size distributions, Corros. Sci. 58 (2012) 133–138.
[68] Y. Jin, R. Li, L. Zuo, T. Zhang, Correlation between dealloying conditions and coarsening behaviors of nanoporous silver produced by chemical dealloying of Ca-Ag metallic glass, J. Alloys Compd. 695 (2017), 600–1609.
[69] E. Detsi, S. Punzhin, J. Rao, P. R. Onck, J. Th. M. De Hosson, Enhanced Strain in Functional Nanoporous Gold with a Dual Microscopic Length Scale Structure, *ACS Nano 6* (5)(2012) 3734-3744.
[70] T. Wada, P.-A. Geslin, H. Kato, Preparation of hierarchical porous metals by two-step liquid metal dealloying, Scr. Mater. 142 (2018) 101-105.
[71] W. Kurtz and K. Fisher, Trans Tech Publications, Switzerland, Fundamentals of solidification, 1998.
[72] F. Yan, W. Xiong, E.J.Faierson, Grain Structure Control of Additively Manufactured Metallic Materials, *Materials* 10 (2017) 1260.
[73] S. Kou, John Wiley & Sons, USA, Welding Metallurgy, 2003.
[74] S.-H. Joo, H. Kato, Transformation mechanisms and governing orientation relationships through selective dissolution of Ni via liquid metal dealloying from (FeCo)xNi100−x precursors, *Materials & Design* 185 (2020) 108271.
[75] D. A. Porter, K. E. Easterling and Mohamed Sherif, CRC presse, Phase transformations in metals and alloys, 2009.

Figure caption

Graphical abstract

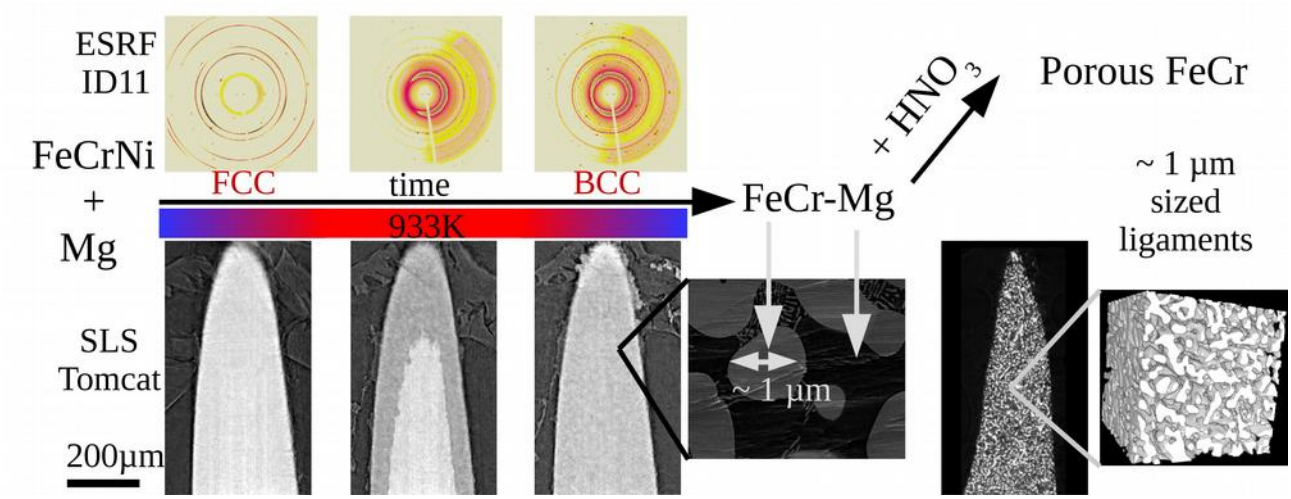

Fig. 1: Evolution of a dealloying front during the dealloying process from $(FeCr)_{30}Ni_{70}$ (a) sagittal slices of the sample at different intervals (b) 3 different horizontal slices at 3 intervals corresponding approximately to the position of the dashed colored line in (a). Black dashed lines correspond to the volume used to quantify the evolution of the dealloying process. Red arrows highlighted some irregularities noticed at the precursor/dealloying part boundaries.

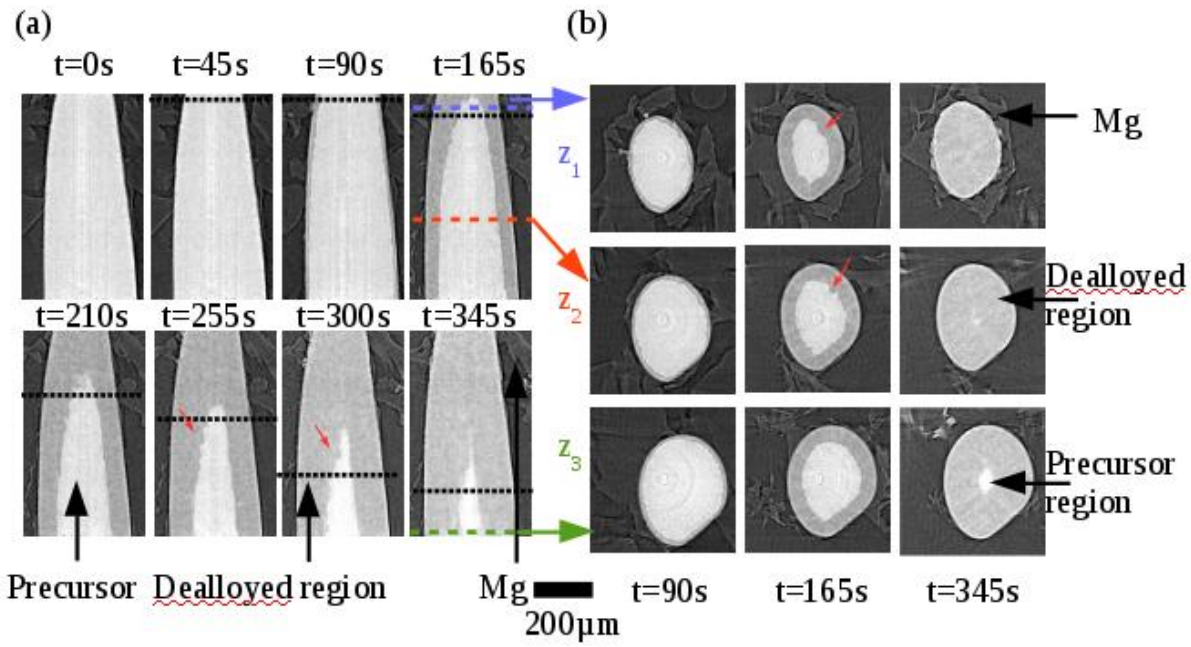

Fig. 2 Evolution of dealloying thickness with time for 2D and 3D measurements (blue axis). The continuous line corresponds to the simulation (black axis).

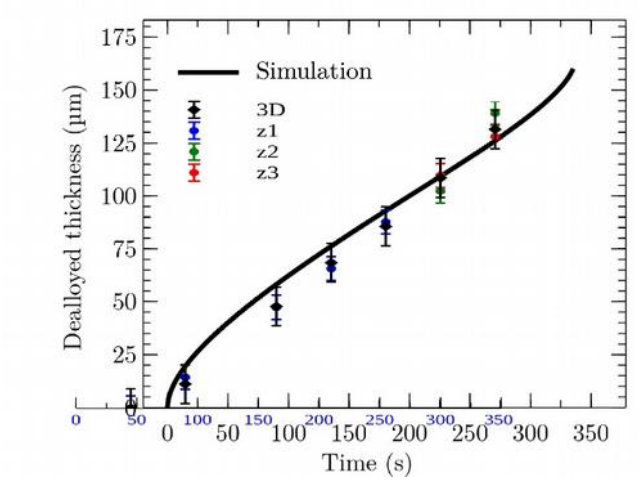

Fig. 3 Evolution of relative strain (continuous lines) and intensity (dashed lines) of 2 different FCC precursors and 2 different BCC dealloyed diffraction peaks during dealloying. The arrows highlight interaction between the 2 phases during the cooling step.

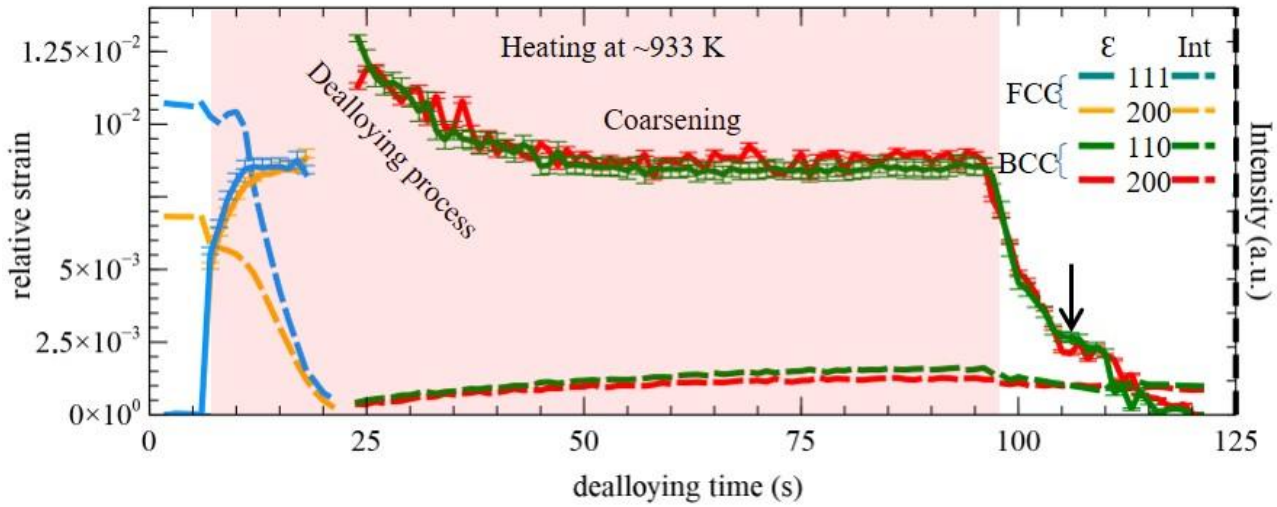

Fig. 4(a) 2D view extracted from a 3D reconstruction for t = 1048 s. The red ellipse highlights a defect (b) Evolution of FeCr and Mg/air-etchant phase thickness during the sacrificial phase etching step. As inset, the evolution of the FeCr phase volume ratio (relative density) is plotted.

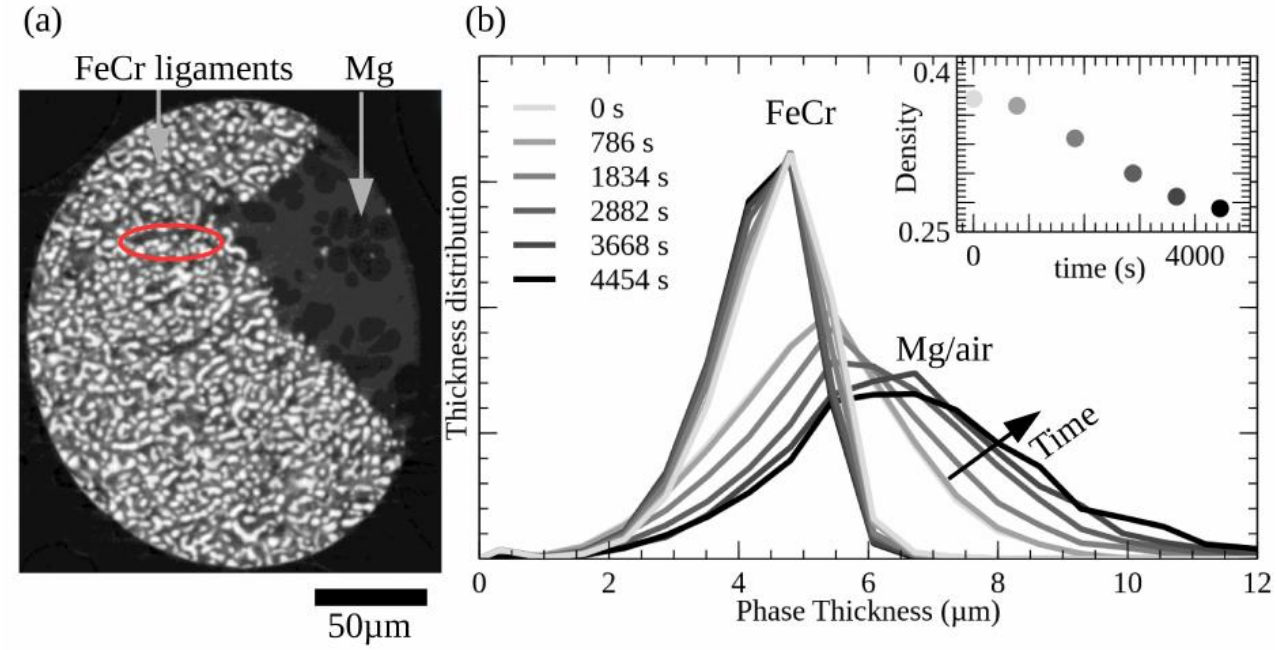

Fig. 5 (a) XRD diffraction pattern after chemical etching (t=1700s) (b) Evolution of the relative lattice parameter during the Mg phase etching of 30%FeCr (red) and 70%FeCr samples (gray).

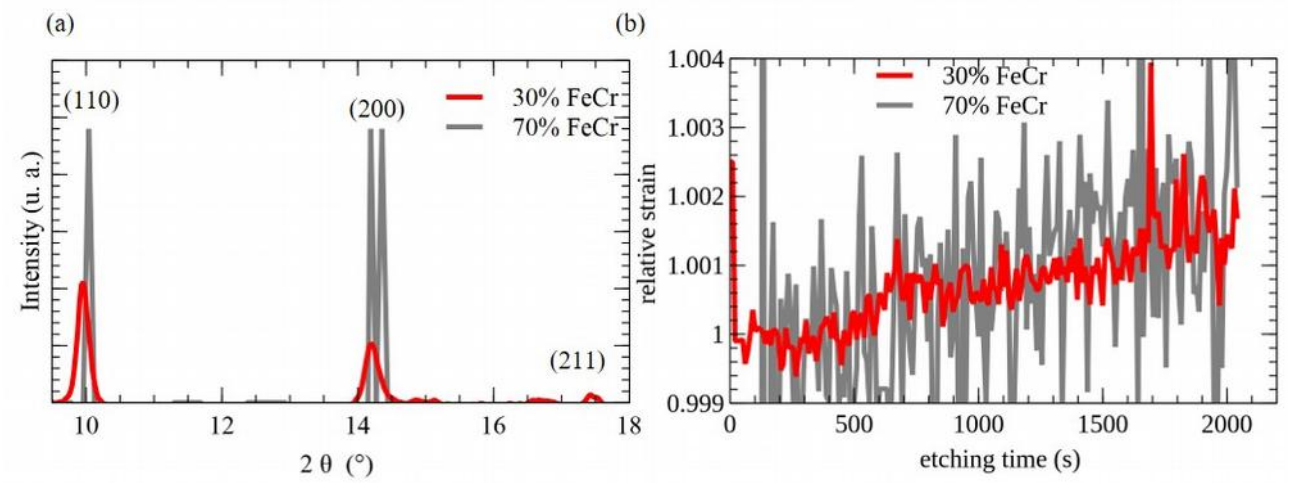

Fig. 6 (a) XRD diffraction pattern of the BCC phase (t=80s) (b) Evolution of relative strain and of BCC dealloyed diffraction peaks (111) during dealloying of a $(FeCr)_{30}Ni_{70}$ (red) and $(FeCr)_{70}Ni_{30}$ (gray) precursors (c) IQ+IPF SEM-EBSD map after 3 mins dealloying at 933 K from $(FeCr)_{30}Ni_{70}$ (left) and $(FeCr)_{70}Ni_{30}$ (right). The bottom part corresponds to the precursor and the top part to dealloyed portion. Arrows correspond to the cold-rolling direction (RD) and dealloying reaction direction (DD).

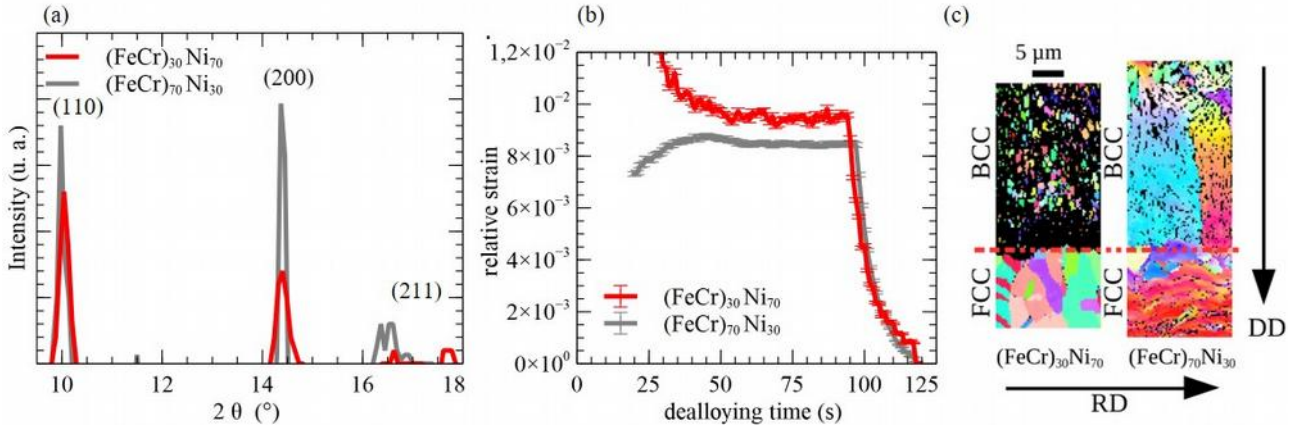

Fig. 7 Grain formation during dealloying. The red part corresponds to the FCC phase. (a) for a low amount of FeCr, the high kinetics of dealloying promotes a morphological transformation with the formation of FCC ligaments followed by a displacive transformation, (b) for a high amount of FeCr, the slow kinetics of dealloying promotes a diffusive transformation with the direct formation of BCC ligament.

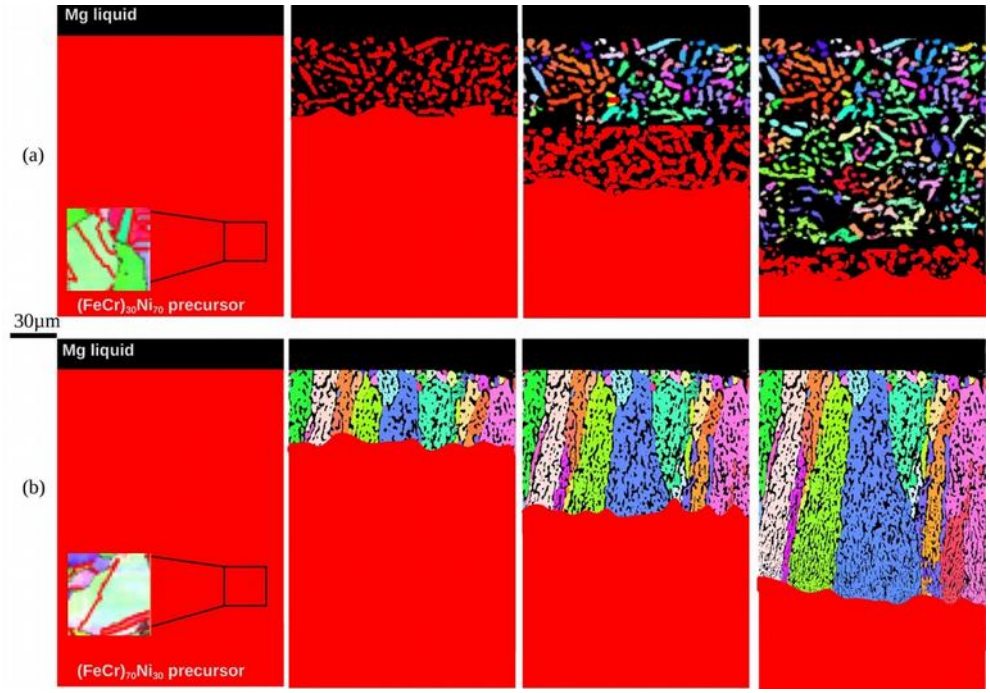

Appendix 1: Illustration of experimental set-up.

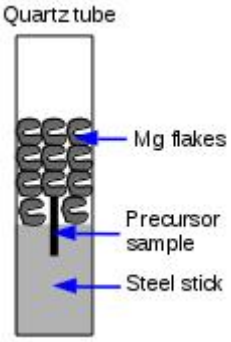

Appendix 2: Sagittal slices extracted from the 3D reconstruction showing the evolution of dealloying front during dealloying process from $(FeCr)_{70}Ni_{30}$ precursor sample. Light gray and median gray correspond respectively to precursor area and to dealloyed area.

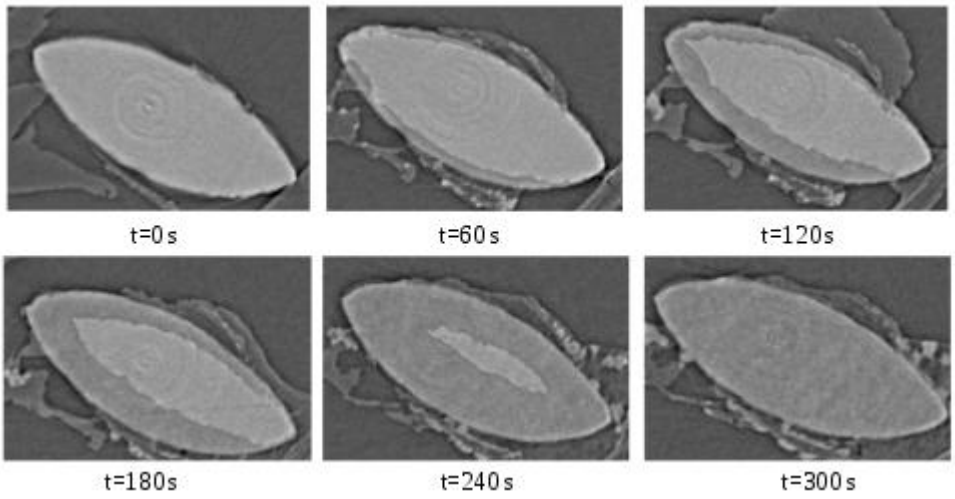

Appendix 3: (a) Evolution of dealloying thickness with time from $(FeCr)_{70}Ni_{30}$ precursor sample. To be able to compare simulation and experimental values, the experimental incubation time was subtracted from the experimental time. The continuous line corresponds to the simulation. (b) Evolution of FeCr and Mg/air phase thickness during sacrificial phase etching step of a dealloyed sample from a $(FeCr)_{70}Ni_{30}$ precursor.